

Quantum-Informed Machine Learning for Chaotic Systems

Maida Wang,^{1, a)} Xiao Xue,^{1, b)} and Peter V. Coveney^{1, 2, 3, c)}

¹⁾*Centre for Computational Science, Department of Chemistry,
University College London, London, UK*

²⁾*Informatics Institute, University of Amsterdam, Amsterdam,
The Netherlands*

³⁾*Centre for Advanced Research Computing, University College London,
UK*

Learning the behaviour of chaotic systems remains challenging due to instability in long-term predictions and difficulties in accurately capturing invariant statistical properties. While quantum machine learning offers a promising route to efficiently capture physical properties from high-dimensional data, its practical deployment is hindered by current hardware noise and limited scalability. We introduce a quantum-informed machine learning framework for learning partial differential equations, with an application focus on chaotic systems. A quantum circuit Born machine is employed to learn the invariant properties of chaotic dynamical systems, achieving substantial memory efficiency by representing these complex physical statistics with a compact set of trainable circuit parameters. This approach reduces the data storage requirement by over two orders of magnitude compared to the raw simulation data. The resulting statistical quantum-informed prior is then incorporated into a Koopman-based auto-regressive model to address issues such as gradient vanishing or explosion, while maintaining long-term statistical fidelity. The framework is evaluated on three representative systems: the Kuramoto–Sivashinsky equation, two-dimensional Kolmogorov flow and turbulent channel flow. In all cases, the quantum-informed model achieves superior performance compared to its classical counterparts without quantum priors. This hybrid architecture offers a practical route for learning dynamical systems using near-term quantum hardware.

Keywords: Quantum Machine Learning; Koopman Operator; Dynamical Systems

^{a)}These authors contributed equally to this work.

^{b)}These authors contributed equally to this work

^{c)}Email: p.v.coveney@ucl.ac.uk

I. INTRODUCTION

Modelling chaotic dynamical systems remains one of the most persistent challenges in computational science. Partial differential equations (PDEs) provide the mathematical backbone for describing a wide range of nonlinear, spatiotemporal processes across scientific domains¹⁻³ and engineering domains⁴. However, chaotic systems are notoriously sensitive to initial conditions and the floating-point numbers used to compute them⁵⁻⁸, making it highly challenging to extract stable, predictive models from data. Modern machine learning techniques often struggle in this regime: while they may fit short-term trajectories, they fail to learn the invariant statistical properties that govern long-term system behaviour. These challenges are compounded in high-dimensional settings, where data are highly nonlinear and contain complex multi-scale spatial-temporal correlations.

Machine learning has seen transformative success in domains such as large language models⁹⁻¹², computer vision¹³⁻¹⁶, and weather forecasting¹⁷⁻²⁰, and is increasingly being adopted in scientific disciplines under the umbrella of scientific machine learning^{21,22}. In fluid mechanics in particular, ML has been used to model complex flow phenomena, including wall modeling^{23,24}, subgrid-scale turbulence^{25,26}, and direct flow field generation^{27,28}. Physics-informed neural networks²⁹ attempt to inject domain knowledge into the learning process, yet even these models struggle with the long-term stability and generalisation issues that chaotic systems demand. To address this, generative models such as Generative Adversarial Networks (GANs)³⁰ and operator-learning architectures like DeepONet³¹ and Fourier Neural Operators (FNOs)³² have been proposed. While neural operators offer discretisation invariance and strong representational power for PDE-based systems, they still suffer from error accumulation and prediction divergence over long horizons, particularly in turbulent or chaotic regimes^{33,34}. Recent work, such as Dyslim³⁵, enhances stability by leveraging invariant statistical measures. However, these methods depend on estimating such measures from trajectory samples, which can be computationally intensive and inaccurate in all forms of chaotic systems. These limitations have prompted exploration into alternative computational paradigms. Quantum machine learning (QML) has emerged as a compelling candidate due to its ability to natively represent and manipulate high-dimensional probability distributions in Hilbert space. Quantum circuits can exploit entanglement and interference to express rich, non-local statistical dependencies using fewer parameters than their classical

counterparts, which makes them well-suited for learning invariant measures in chaotic systems, where long-range correlations and multimodal distributions frequently arise³⁶. QML has already demonstrated potential in fields such as quantum chemistry^{37–40}, combinatorial optimisation^{41–43}, and generative modeling^{44–47}. However, fully quantum approaches remain constrained by current hardware limitations, such as noise, low qubit counts, and the difficulty of encoding classical physical systems into quantum circuits⁴⁸. These challenges limit the standalone utility of QML in scientific applications today. Instead, hybrid quantum–classical models provide a promising compromise, where quantum submodules are embedded into classical learning pipelines to improve expressivity, data efficiency, and physical fidelity without relying on fault-tolerant quantum computers. Consequently, hybrid architectures have emerged as a promising compromise, enabling practical impact even with noisy intermediate-scale quantum (NISQ) devices. Rather than relying on fully quantum pipelines, these approaches embed quantum modules into classical learning systems to exploit quantum expressivity while retaining classical scalability and training robustness. In quantum chemistry, this hybrid paradigm has proven feasible, notably through quantum mechanical/molecular mechanical (QM/MM) coupling^{49–51}, where classical force fields are augmented with quantum corrections. Within such frameworks, techniques like quantum-selected configuration interaction (QSCI)⁵² have been employed to enhance accuracy while keeping quantum resource requirements tractable.

Here, we propose a Quantum-Informed Machine Learning (QIML) architecture for learning chaotic dynamical systems. At the core of QIML is a quantum circuit Born machine (QCBM)^{53,54}, which is trained on superconducting quantum hardware to learn invariant statistical properties directly from observational data. These properties capture complex, high-dimensional distributions compactly by leveraging entangled quantum states. Unlike standard deep-learning surrogates, such as fully connected or convolutional networks that require large parameter counts to represent such structures, QCBMs operate in exponentially large Hilbert spaces, enabling expressive modelling with as few as 10 to 15 qubits. Crucially, this framework circumvents the data-loading bottleneck common to many quantum machine learning algorithms. The QCBM does not need to encode raw data onto quantum states; instead, it learns a compressed, generative model of the data’s underlying statistical properties. The model is trained with a sample-based Maximum Mean Discrepancy (MMD) loss⁵⁵, enabling it to learn the quantum representation without knowing the data distribu-

tion. The resulting quantum prior (Q-prior) is a highly memory-efficient “quantum device interpreter” that captures the system’s essential statistics in a compact set of parameters in quantum circuits. The data storage requirement is consistently reduced by over two orders of magnitude across the studied systems when using the Q-priors instead of the raw simulation data. The resulting Q-prior is then embedded into a Koopman-based machine learning model, guiding it to maintain long-term statistical fidelity while mitigating autoregressive instabilities such as gradient vanishing or explosion. The QIML framework is implemented as a modular pipeline that integrates quantum-generated priors into a differentiable classical loss⁵⁶. This enables joint optimisation of statistical consistency and dynamical fidelity, including full compatibility with existing superconducting quantum hardware. Even without achieving full quantum advantage⁵⁷, the inclusion of Q-priors significantly improves parameter efficiency, prediction stability, and statistical alignment in high-dimensional chaotic regimes. This work demonstrates that QIML provides a practical and scalable hybrid solution for scientific machine learning: one that leverages quantum expressivity while remaining compatible with the practical constraints of current quantum hardware.

In this work, we present the QIML architecture that leverages a quantum-classical hybrid approach for machine learning-based modelling of chaotic dynamical systems. Our QIML scheme is illustrated in Fig. 1. The workflow commences with the data generation stage (Fig. 1a), where we employ a numerical solver on a classical computer to simulate complex chaotic flows, producing the necessary training, validation, and testing datasets. Subsequently, in the quantum machine learning phase (Fig. 1b), a QCBM is implemented on a quantum computer to learn the underlying physical invariant distribution, referred to as the Q-prior. Finally, this Q-prior is used to inform and regularise the classical machine learning model during training (Fig. 1c), guiding it toward long-term statistical consistency with the target dynamical system. The proposed integration demonstrates both practical feasibility and scalability, marking a step towards applying quantum modules in the learning of non-linear partial differential equations. We demonstrate the scalability and robustness of the solution of the QIML framework across a hierarchy of increasingly complex chaotic dynamical systems. First, we evaluate the model on the Kuramoto–Sivashinsky (KS) equation. The solution is discretised into 512 spatial grid points, resulting in a 512-dimensional state vector at each time step. Next, we extend our study to a two-dimensional Kolmogorov flow on a 64×64 spatial grid, where the QCBM is trained in simulation to extract turbulent invariant

measures. Finally, we validate the framework on a cross-section of a three-dimensional turbulent channel flow (TCF). The QCBM is trained on superconducting quantum processors. This progression demonstrates the generality and hardware compatibility of QIML. In all cases, our QIML models outperform classical counterparts lacking Q-prior, particularly in terms of long-term prediction stability, statistical fidelity, and resilience to error accumulation. Crucially, the QCBM acquires these priors directly from raw samples, so the framework remains applicable even when the invariant measure of a high-dimensional chaotic system is unknown. We provide concrete demonstrations of how quantum and classical machine learning can be synergistically combined to address high-dimensional dynamical systems.

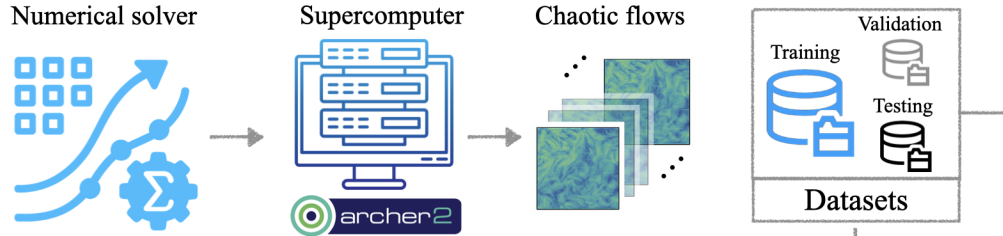
II. APPLICATIONS

The selected test cases span increasing levels of physical and dynamical complexity. We begin with the Kuramoto–Sivashinsky equation, a one-dimensional PDE exhibiting spatiotemporal chaos. Next, we consider two-dimensional Kolmogorov flow, governed by the 2D incompressible Navier–Stokes equations in a periodic domain. Finally, we examine cross-sections of a three-dimensional turbulent channel flow, simulated using the lattice Boltzmann method (LBM), which is numerically equivalent to solving the Navier–Stokes equations⁵⁸. While the full flow field is simulated numerically, the extracted two-dimensional cross-sectional datasets used in our analysis do not satisfy any closed-form governing equation. This distinction highlights a further step in complexity: moving from lower-dimensional systems with explicit dynamics to high-dimensional observational data without accessible evolution laws, thereby testing the capacity of QIML to generalise across different scenarios.

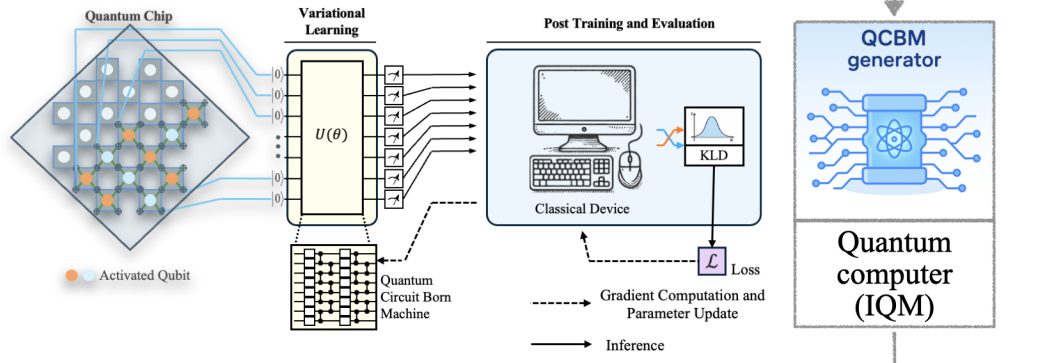
Throughout this study, ‘ground truth’ or ‘raw data’ refers to the high-resolution simulation data generated by established numerical solvers. While this raw simulation data has a large memory footprint, the quantum-informed priors offer substantial memory efficiency. They capture the flow’s essential statistical features using fewer than 300 trainable parameters, occupying only a few megabytes of storage, which corresponds to a data storage reduction of over two orders of magnitude compared to the raw data. This approach enables a substantial reduction in data storage requirements compared to using the raw simulation data (see section Method E and Supplementary Sections S2–S3). The classical components of the models were trained on a single NVIDIA A100 80GB GPU using default settings with

The Structure of the Quantum-Informed Machine Learning

a. Data generation



b. QCBM for Q-prior learning



c. Quantum-informed surrogate learning

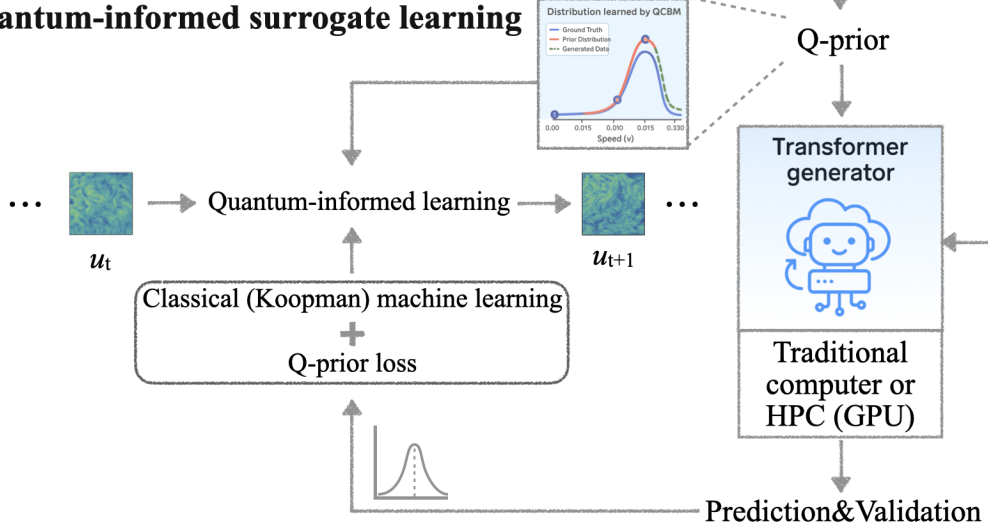


FIG. 1. **Architecture of the QIML framework.** **a.** Chaotic flow fields are generated using high-resolution numerical solvers and used to construct training, validation and test datasets. **b.** A QCBM is trained on superconducting hardware to learn invariant statistical properties from the data (Q-prior). **c.** The learned Q-prior is integrated into a classical Koopman-based transformer surrogate, guiding it toward physically consistent predictions and improved long-term stability.

32-bit floating-point precision (for details see Supplementary Section S4.3).

A. Kuramoto-Sivashinsky equation

We first apply our QIML framework to learn the solution of the Kuramoto-Sivashinsky equation, which is given by:

$$\frac{\partial u}{\partial t} + u \frac{\partial u}{\partial x} + \nu \frac{\partial^2 u}{\partial x^2} + \mu \frac{\partial^4 u}{\partial x^4} = 0 \tag{1}$$

where $u(x, t)$ denotes a scalar field representing the state of the system, with $u : [0, L] \times [0, \infty) \rightarrow \mathbb{R}$, $x \in [0, L]$ representing the spatial domain and $t \in [0, \infty)$ the time; ν and μ are constants which are set to 1 for this study. The spatial domain is discretised using $N = 512$ equidistant grid points. Raw data are generated as described in Supplementary Information S4.1. The dataset consists of 1200 trajectories, where each trajectory is made up of 2,000 time frames. The spatial domain for each frame is discretised using 512 grid points. We partition the trajectories chronologically into 80 % training, 10 % validation, and 10 % test sets. For this system, both the classical Koopman surrogate (without Q-prior) and the main QIML model (with Q-prior) are trained for 500 epochs. The Q-prior for the QIML configuration is generated by a QCBM using 10 qubits ($2^{10} = 1\,024$ basis states) and 120 trainable parameters. Full architectural and training details for both configurations are provided in Supplementary Information S7.

Fig. 2 presents the QIML evaluation results on the Kuramoto–Sivashinsky system, comparing two configurations against the numerical simulation: a classical surrogate model trained without Q-priors (without Q-prior), and a quantum-informed surrogate model incorporating a QCBM prior trained in simulation (with Q-prior). Both surrogate models perform inference in an auto-regressive manner: starting from an initial condition at time step $t_0 = 0$, the model predicts the next frame at each subsequent step and recursively continues this process up to $t_{\text{end}} = 500$ time steps to ensure long-term statistics. Panel (a) shows the u evolution alone the time: with 512 initial states and 500 prediction timesteps and the corresponding relative error E_r evolution. The error metric definition is presented in Supplementary S9. From top to bottom, each row corresponds to the ground truth, the ML model without Q-prior configuration, and the QIML model with Q-prior configuration. These sub-panels are computed over the test dataset to visualize long-term statistical characteristics of the predictions. In the “without Q-Prior” configuration, the model reproduces

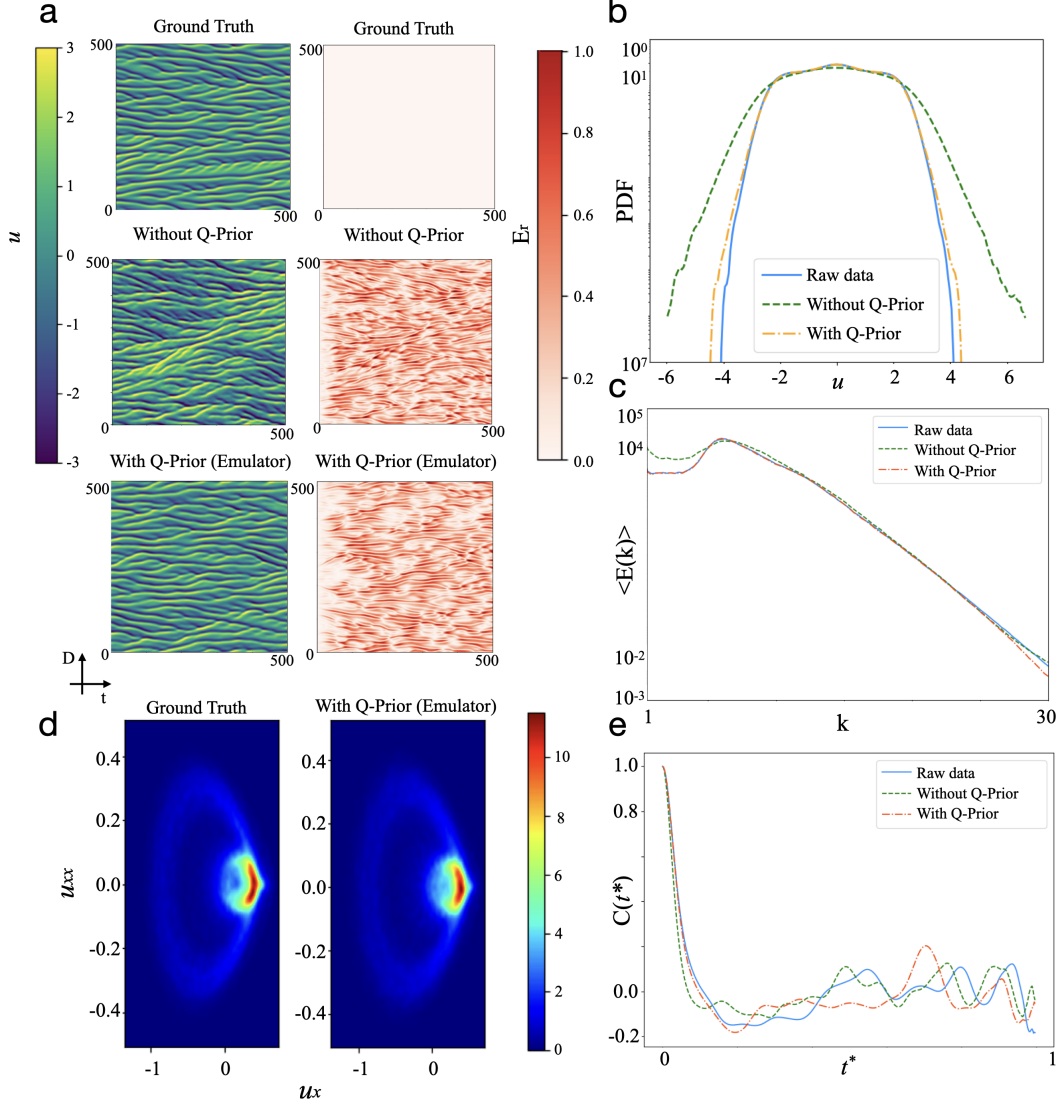


FIG. 2. **Evaluation of the QIML framework on the KS system.** **a.** This panel displays time-averaged mean velocity fields (left column) and corresponding relative error E_r maps (right column) across the ground truth, the classical ML without Q-prior, and the quantum-informed ML model with Q-prior (from top to bottom). **b.** This panel presents the probability distribution of u . **c.** This panel shows the one-dimensional energy spectrum $\langle E(k) \rangle$ as a function of spatial wavenumber k , characterizing kinetic energy distribution across spectral modes. **d.** This panel visualizes the invariant density when dynamics are projected into the (u_x, u_{xx}) space, revealing the geometric support of the underlying invariant measure. **e.** This panel plots the temporal autocorrelation, denoted by $C(t^*)$, computed from the time series of the field u averaged over all spatial points. The correlation is shown as a function of the dimensionless time lag $t^* = t/t_{end}$.

the general structure of the ground truth. However, over time, the predicted stripe patterns drift upward, revealing noticeable discrepancies in the associated error map. This indicates that the model accumulates errors during long-term prediction, likely due to the absence of prior information to guide the dynamics. In contrast, the “with Q-Prior” model demonstrates much closer alignment with the ground truth. The predicted fields preserve fine-scale features and capture the parallel stripe structures effectively. Additionally, the corresponding error maps exhibit substantially lower and more spatially diffuse errors. These results suggest that incorporating the Q-Prior enhances the model’s stability and accuracy in long-term forecasting. Panel (b) presents the probability density function (PDF) of u for each configuration. The distribution is obtained via the entire spatiotemporal test domain (512 states in space and 500 prediction steps in time), allowing for a comparison of global statistical fidelity. The raw test data (solid blue line) serves as the ground truth. The model without Q-Prior (green dashed line) deviates from the raw data, particularly in the tails of the distribution, where it tends to overestimate the probability. In contrast, the model with Q-Prior (orange dash-dotted line) closely matches the ground truth across the full velocity range, especially in the tails. This demonstrates that incorporating the Q-Prior generated by the quantum emulator allows the surrogate model to more accurately reproduce the statistical characteristics of the system, including rare events. Panel (c) shows the energy spectrum $\langle E(k) \rangle$ as a function of the wave number k , comparing the raw data, the surrogate model with and without Q-Prior. The energy spectrum of the raw data follows a smooth decay with increasing k , reflecting the distribution of energy across spatial frequencies. The model without Q-Prior overestimates the energy in the large-scale, deviating from the ground truth. However, the model with Q-Prior closely aligns with the raw data across all wave numbers, able to capture both large scale and small-scale (high- k) behaviour of the system. To further visualize the invariant structures underlying the KS system, we project both the ground truth and the Q-Prior configuration into the (u_x, u_{xx}) phase space, as shown in Panel (d). The resulting density plots depict the support of the system’s invariant measure, providing insight into its long-term statistical behaviour. Over extended prediction, the model with Q-Prior closely aligns with the ground truth in phase space, accurately capturing the geometry and concentration of the invariant set. This qualitative agreement highlights the Q-Prior model’s ability to preserve the system’s underlying statistical structures over time. Panel (e) illustrates the temporal autocorrelation $C(t^*)$ of the

velocity field, averaged over all spatial points, as a function of the dimensionless time lag $t^* = t/t_{end}$. Autocorrelation measures how strongly the system retains correlation with its past states over time. Specifically, its calculation is presented in Supplementary S9. In this plot, all cases exhibit a decay in autocorrelation, eventually showing no correlation with the initial state. The configuration with Q-Prior demonstrates stronger short-term correlation (the same as the ground truth data) compared to the model without Q-Prior, indicating better preservation of temporal dynamics in the early prediction period. These outcomes demonstrate that our designed Q-prior can regularise the classical ML model, preserving both long-scale and small-scale structures, and improving long-term statistical accuracy.

B. 2D Kolmogorov flow

Next, we apply our QIML framework to learn the dynamics of the 2D Kolmogorov flow, a canonical example of incompressible Navier-Stokes dynamics under sinusoidal forcing. The governing equations are:

$$\frac{\partial \mathbf{u}}{\partial t} + (\mathbf{u} \cdot \nabla) \mathbf{u} = -\nabla p + \nu \nabla^2 \mathbf{u} + \mathbf{F}, \quad (2)$$

$$\nabla \cdot \mathbf{u} = 0, \quad (3)$$

where \mathbf{u} is the velocity field, p represents the pressure. Here \mathbf{u} denotes the velocity field on the 2D cases. In the algorithmic expressions, we revert to the simpler symbol u , using it as a generic placeholder for both 1D scalar and 2D velocities, since the learning procedure applies uniformly across dimensionalities. ν is the kinematic viscosity, and the forcing term is given by $\mathbf{F}(x, y) = (F \sin(ky), 0)$ for some amplitude F and wave number k . The domain is periodic in both x and y directions: $(x, y) \in [0, L_x] \times [0, L_y]$ with $L_x = L_y = 64$ grids. The data source is presented in Supplementary Information S4.2. We use 80% for training, 10% for validation, and 10% for testing. For this system, both the classical Koopman surrogate (without Q-prior) and the main QIML model (with Q-prior) are trained for 500 epochs. For QIML, the QCBM uses $n = 10$ qubits ($2^{10} = 1024$ basis states) and 180 trainable parameters. Detailed network architectures, training hyperparameters, and data generation procedures are provided in Supplementary Information S7.

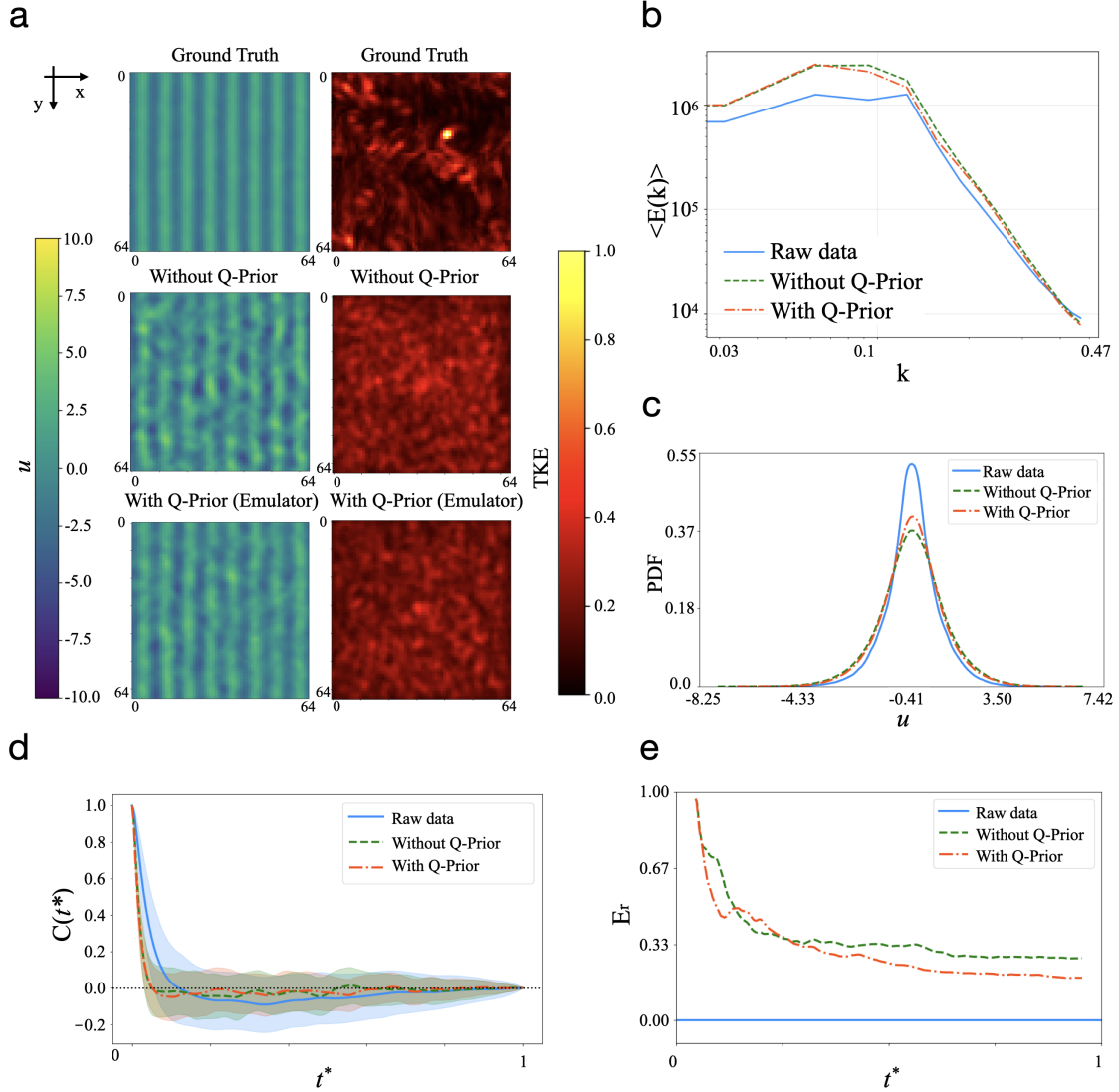


FIG. 3. **Evaluation of the QIML framework on the 2D Kolmogorov flow.** **a.** This panel displays time-averaged mean u fields (left column) and corresponding TKE fields (right column) for the ground truth, the classical model without Q-prior, and the quantum-informed model with Q-prior. These maps are evaluated on the test set, highlighting long-term flow patterns and energy distribution. **b.** This panel presents the ensemble-averaged energy spectrum $\langle E(k) \rangle$ as a function of spatial wavenumber k . **c.** This panel shows the PDF of the field variable u , comparing the distribution from the raw test data with the PDFs predicted by the models with and without the Q-prior. **d.** This panel plots the temporal autocorrelation $C(t^*)$ of the velocity field as a function of dimensionless time t^* . **e.** This panel reports the normalized relative error, E_r , with respect to the ground truth, calculated over time on the same validation trajectory for 1000 steps roll out.

Figure 3 reports the comparative performance of the baseline ML model (without Q-prior) and the quantum-informed ML model (with Q-prior) on the two-dimensional Kolmogorov flow dataset. Panel (a) shows the time-averaged velocity field and the corresponding turbulent kinetic energy (TKE) field across three configurations: the ground truth from simulation, the classical model trained without Q-prior, and the quantum-informed model trained with Q-prior. All models are evaluated on the same test data. Both the “with Q-Prior” and “without Q-Prior” models perform auto-regressive (one frame in one frame out) inference over a horizon of $t_{end} = 1000$ time steps. The visualisations span a two-dimensional domain of size 64×64 in the x - y plane. The time-averaged velocity field is plotted on the left column and the corresponding TKE field is shown on the right column. The ground truth velocity field (top left) exhibits coherent, stripe-like structures, and its TKE field (top right) reveals concentrated regions of high energy, indicating the presence of organized flow features. The model without Q-Prior (middle row) shows degraded spatial coherence in the velocity field, with disrupted patterns and more noise-like structures. In contrast, the model with Q-Prior (bottom row) recovers a more organized velocity field, better preserving the stripe patterns observed in the ground truth. Its associated TKE field also aligns more closely with the ground truth. Panel (b) presents the ensemble-averaged energy spectrum $\langle E(k) \rangle$ as a function of the wavenumber k for the raw data (solid blue line), the surrogate model without Q-Prior (green dashed line), and the model with Q-Prior (orange dash-dotted line). The spectrum from the model without Q-prior overestimates the energy spectrum at low and intermediate wave numbers. However, the Q-prior aligns closer to the raw data across the whole spectrum. Then, we further examine the overall velocity distributions. As illustrated in Panel (c), we compare the predicted velocity probability density functions from both surrogate models. The raw data exhibit a sharply peaked distribution with heavy tails, characteristic of the system’s inherent velocity fluctuations. Both surrogate models capture the general symmetric shape of the distribution but tend to slightly underestimate the peak and overestimate the spread. Among them, the model with Q-Prior more closely matches the raw data, particularly around the peak and in the tails, indicating improved accuracy in reproducing the system’s statistical behaviour. These results further support the conclusion that incorporating the Q-Prior enhances the surrogate model’s ability to recover velocity statistics. We also examined the auto-correlation of the field along time. Panel (d) plots the autocorrelation $C(t^*)$ of the velocity field as a function of dimensionless

time $t^* = t/t_{end}$. The correlation is computed over 100 randomly sampled locations, with shaded regions indicating one standard deviation. Both surrogates reproduce long-term decay in autocorrelation followed by fluctuations around zero, consistent with the expected loss of memory in a chaotic or turbulent system. To further analyse the model, Panel (e) reports the normalised relative auto-correlation error E_r with respect to the ground truth. The raw data serves as the reference baseline with zero error. The model without Q-Prior shows a gradual decrease in relative error over time but maintains a consistently higher error floor. In contrast, the model with Q-Prior exhibits a more rapid reduction in normalized relative error and achieves lower relative error throughout the prediction horizon.

These observations confirm that the quantum-informed Q-prior can supply additional information that improves classical ML fidelity and velocity statistics, and enhances long-horizon accuracy.

C. Turbulent Channel Flow Inflow Generation

We further evaluate our QIML framework on turbulent channel flow, a representative case of wall-bounded turbulence. In this setting, the training data is obtained from the mid-plane cross-section of a fully developed periodic turbulent channel flow at friction Reynolds number $Re_\tau = 180$. Note that the reference data has been validated with the DNS data⁵⁹ (See supplementary information S5.5). The reference data is generated using the LBM solver, which serves as an efficient alternative to directly solving the Navier-Stokes equations^{58,60}. A large eddy simulation (LES) formulation is employed to capture the large-scale turbulent structures^{24,61}. The governing equations used for generating the data are provided in the Supplementary Information S.5. The detailed description of the data generation setup is described in Supplementary Information S.8.3. The channel flow snapshots are split 80:10:10 into training, validation and test sets. For this system, both the classical Koopman surrogate (without Q-prior) and the main QIML model (with Q-prior) are trained for 500 epochs. For QIML, we employ a 15-qubit QCBM ($2^{15} = 32\,768$ basis states) with 240 trainable parameters. Detailed network architectures, training hyperparameters, and data generation procedures are provided in Supplementary Information S7.

Fig. 4 presents the evaluation of the quantum-informed machine learning framework on the turbulent channel flow dataset. Our ML models perform auto-regressive (one frame in

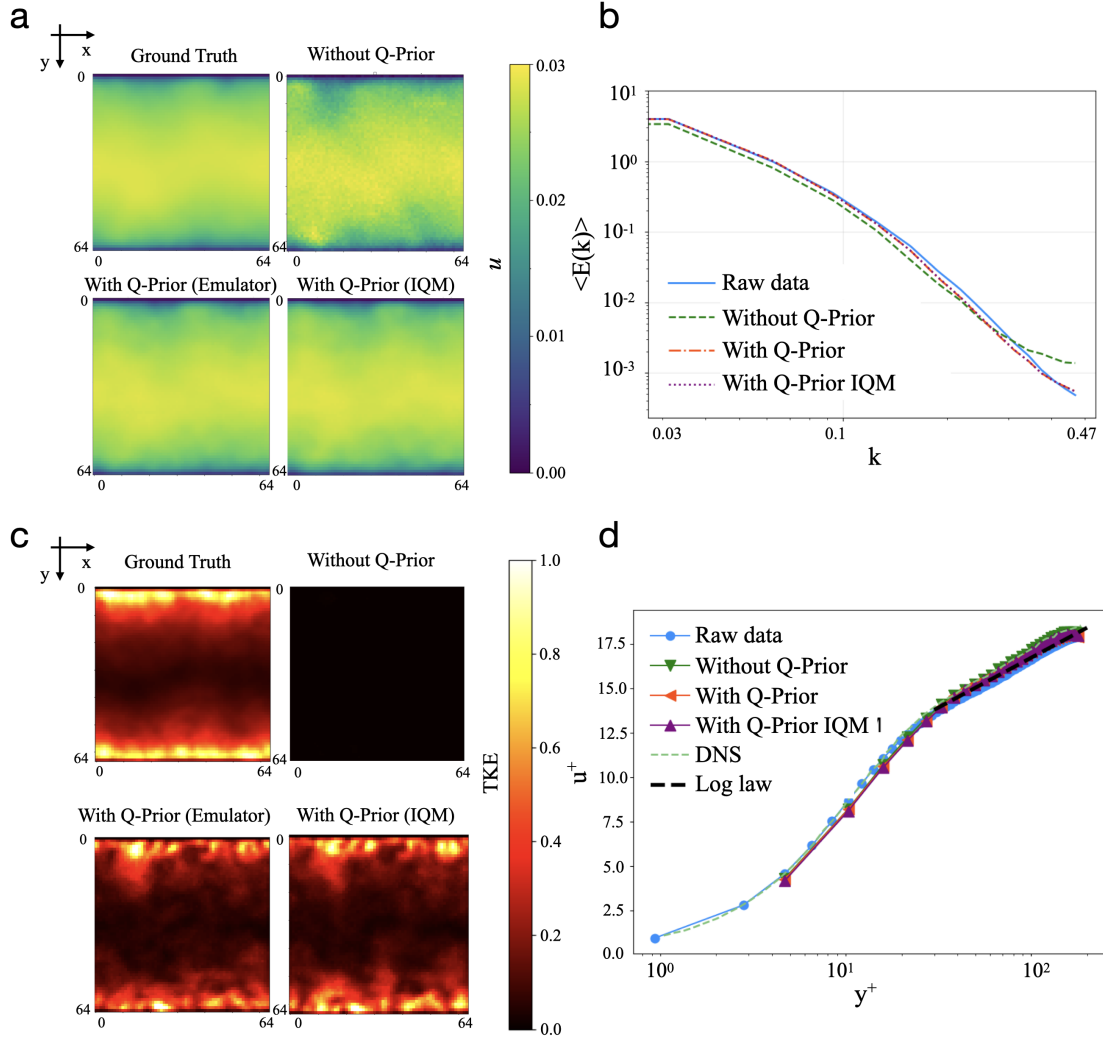


FIG. 4. **Evaluation of the QIML framework on the TCF system.** **a.** This panel displays time-averaged streamwise velocity fields across different models. Each row corresponds to a different model output: the top row displays the ground truth obtained from DNS, followed by results from the classical model without Q-prior, the QIML model using Q-prior trained on Emulator, and the model using a Q-prior trained on real superconducting hardware (IQM). **b.** This panel plots the ensemble energy spectrum $\langle E(k) \rangle$ as a function of the spatial wavenumber k . **c.** This panel displays the time-averaged TKE field for the same four configurations as in Panel (a), using a normalized colour scale to enhance visual comparability. **d.** This panel shows the non-dimensional velocity profile u^+ as a function of the wall-normal coordinate y^+ on a logarithmic scale. Results are compared with the empirical log-law and DNS reference, using the same validation data as in previous panels.

one frame out) inference over a horizon of $t_{end} = 1000$ time steps. The visualisations span a two-dimensional domain of size 64×64 in the x - y plane. Panel (a) shows a comparison of time-averaged velocity magnitudes u across a 64×64 domain for the ground truth, the surrogate model without Q-Prior, and two Q-Prior-enhanced variants: the emulator and real superconducting IQM device. The colourbar on the right indicates the magnitude of u , with higher values in yellow and lower values in blue. The ground truth (top left) displays smooth large-scale variations in the velocity field. The model without Q-Prior (top right) introduces noticeable small-scale noise and fails to capture the smooth gradients seen in the true field. In contrast, both Q-Prior (with emulator and with IQM device) models (bottom row) closely match the ground truth, preserving the dominant spatial structures and exhibiting lower spurious variability. Panel (b) plots the ensemble energy spectrum $\langle E(k) \rangle$ as a function of the wavenumber k for the raw data (solid blue line), the surrogate model without Q-Prior (green dashed line), the model with Q-Prior (orange dash-dotted line), and the model with Q-Prior IQM (purple dotted line). The model without Q-Prior deviates from the ground truth at higher wavenumbers, with discrepancies arising at smaller spatial scales. In contrast, both Q-Prior variants better capture the energy distribution across all scales. Panel (c) compares the normalised TKE fields across a 64×64 spatial domain for the ground truth, the model without Q-Prior, and two Q-Prior-based configurations: the Emulator and IQM. The ground truth (top left) displays spatially structured regions of elevated TKE, particularly near the domain boundaries, reflecting characteristic flow features. The model without Q-Prior (top right) fails to capture any meaningful TKE patterns, instead producing a near-zero field, which indicates an almost static prediction over time. In contrast, both Q-Prior-based models (bottom row) recover structured TKE fields that closely resemble the ground truth. These models preserve the dominant energy distribution and capture the spatial organization of turbulent structures more accurately. Panel (d) shows the dimensionless velocity profile u^+ as a function of the dimensionless wall-normal coordinate y^+ . Results are compared with the raw data, log-law and DNS reference. All surrogates reproduce the canonical log-law behaviour and match well with the reference data, DNS data and log law.

Overall, the Q-Prior provides a clear improvement in the spatiotemporal prediction of cross-sections in turbulent channel flow, where governing equations for the cross-sectional dynamics are not explicitly defined. This makes it a potentially valuable tool for engineer-

ing applications that rely on coupling Reynolds-Averaged Navier–Stokes (RANS) and LES approaches⁶¹.

Collectively, these results demonstrate that embedding Q-priors significantly improves long-term prediction results and statistical alignment of classic machine learning models in chaotic systems. Even with modest quantum resources, that is no more than 15 qubits and under 300 parameters (specifically shown in method F, Supplementary Information S2.2 and S2.3), our framework captures essential dynamics of high-dimensional flows and enables practical hybrid learning pipelines for scientific applications. By anchoring predictions to Q-prior, the QIML model improves statistical fidelity and stability, laying the groundwork for practical quantum–classical synergies in the modelling of turbulent and other chaotic physical systems.

III. DISCUSSION

This work introduces a quantum-informed machine learning framework for learning chaotic dynamical systems. In QIML, a QCBM is trained on superconducting hardware to learn invariant statistical properties from high-dimensional flow data, and the resulting Q-prior is integrated with a classical transformer-based machine learning model. The QIML framework is validated across three representative chaotic systems, demonstrating consistent improvements in long-term stability, physical interpretability, and statistical fidelity compared to classical baselines without Q-prior. The consistent improvements across qualitatively distinct systems suggest that the proposed architecture generalises well and may be adapted to a broader class of nonlinear dynamical systems.

A central contribution of this work lies in its demonstration of parameter-efficient learning. Using fewer than 300 trainable parameters, the QCBM captures statistical distributions over a state space with more than 30,000 dimensions. This parameter economy arises because the QCBM explores a high-dimensional Hilbert space, allowing it to learn long-range velocity correlations with only a few hundred rotation angles. Crucially, the model is trained with a sample-based MMD loss, so it can infer these correlations directly from finite trajectories without requiring an explicit form of the underlying, often unknown, probability density. The proposed QIML architecture establishes a scalable and hardware-compatible pathway for embedding Q-priors into classical machine learning pipelines. By separating

the learning of invariant flow statistics from the time-stepping dynamics, and compressing these complex statistics into highly memory-efficient Q-priors, the framework improves both generalisation and training stability without requiring full end-to-end optimisation. Nonetheless, limitations remain. To reduce the impact of hardware noise and enable stable training, the QCBM is optimised separately and remains fixed during the training of the classical model. This architectural constraint arises from the limited scalability and noises of current superconducting devices, which make full end-to-end quantum training infeasible at present. Although integrated as a static distributional prior, the QCBM captures complex statistical structures, potentially including entanglement, that would require a large amount of classical parameters to approximate. While current QCBMs are limited by qubit count, circuit depth, and hardware noise, deeper architectures with structured entanglement (e.g. hardware-efficient ansätze) may further improve expressivity for highly anisotropic distributions.

While this work demonstrates improvements in learning from digitally generated chaotic system data, we acknowledge the inherent limitations of digital computing in fully capturing the true continuum behaviour of chaotic systems⁵⁻⁸. Our ground truth here is, by definition, a 32 bit floating-point approximation. Future work will explore the use of analogue computation to provide a more direct comparison with the true invariant measures, thus offering a more rigorous validation of our approach against the ultimate ground truth.

QIML demonstrates that even current NISQ devices can contribute meaningfully to the modelling of high-dimensional dynamical systems. Without resorting to fault-tolerant hardware, lightweight quantum modules enhance classical surrogates by providing data-driven Q-priors that efficiently capture complex statistical structures and non-local correlations—features that are otherwise challenging for classical methods to acquire with comparable memory efficiency. The resulting gains in statistical fidelity and long-horizon stability, coupled with a substantial reduction in data storage requirements, point to an immediate and practical role for near-term quantum resources in scientific machine learning. The compact 10- to 15-qubit QCBM presented here exemplifies how such modules can be effectively integrated today. Looking forward, the hybrid architecture introduced here serves as an intermediate but essential step toward fully realising quantum machine learning pipelines. While our current framework integrates quantum priors into classical surrogate models, we envision future extensions in which quantum circuits not only generate priors but also

perform end-to-end learning and generation. Given the exponentially larger Hilbert space accessible to quantum systems, such models are expected to possess superior expressivity for learning high-dimensional generative tasks. As quantum hardware continues to advance, in terms of qubit count, coherence time, and error mitigation, the prospect of replacing classical generative backbones with fully quantum circuits becomes increasingly viable. Thus, the parameter and memory efficiency demonstrated in this work suggest a pathway for quantum modules to ultimately replace entire sections of large classical models.

Furthermore, this hybrid architecture lays the groundwork for a future paradigm of highly efficient information transfer within large-scale, hybrid GPU-QPU infrastructures. As quantum devices advance, one can envision a scenario where highly compressed Q-priors, containing essential physical statistics, are transferred between compute nodes in place of voluminous classical datasets, which are riddled with spurious correlations⁶². This mechanism offers a scalable solution for future large-data training and provides a foundation for progressively more capable quantum-native surrogates as the hardware matures.

IV. METHODS

A. Quantum-informed machine learning framework for chaotic dynamical systems

In this section, we present our QIML framework designed to model and predict the long-term behaviour of chaotic dynamical systems. The framework combines classical machine learning with a quantum generative model. We begin by introducing the machine learning component, which is based on a Koopman operator formulation. The Koopman operator offers a linear representation of nonlinear dynamical systems by acting on observables instead of directly on the state variables. In this framework, the evolution of the system is captured not in the original state space, but in a lifted function space where the dynamics become linear. Consider a discrete-time dynamical system:

$$x_{t+1} = f(x_t), \tag{4}$$

where $x_t \in \mathbb{R}^n$ with n denotes the dimension of the state space at time t , and f is a generally nonlinear transition function. To enable auto-regressive prediction and long-term rollouts,

we aim to find a mapping from the high-dimensional space to a latent space where a linear operator governs the time evolution. The measure-preserving property at the latent space is particularly important for capturing the statistical properties and invariant measure μ of chaotic systems. The Koopman operator K acts on observables $g : \mathbb{R}^n \rightarrow \mathbb{C}$ such that:

$$(Kg)(x) = g(f(x)). \quad (5)$$

While K is linear, our implementations seek finite-dimensional approximations by learning a set of observables whose evolution under K is closed and linear. Next, we approximate the Koopman operator using a neural network; we define an encoder $\phi : \mathbb{R}^n \rightarrow \mathbb{R}^l$, with l denotes the latent dimension, that maps the system state into a latent (feature) space, and a decoder $\psi : \mathbb{R}^l \rightarrow \mathbb{R}^n$ that reconstructs the original state. Unlike generic autoencoders primarily focused on data reconstruction, our Koopman operator neural network is specifically designed to learn a linear, norm-preserving evolution in the latent space, which is crucial for maintaining the long-term stability and physical fidelity of chaotic systems. Our detailed autoencoder-decoder architecture description can be found in Supplementary Information S7.2 and S7.3 for 1D and 2D cases. The dynamics in the latent space are modelled by a linear operator $K \in \mathbb{R}^{l \times l}$, such that:

$$z_t = \phi(x_t), \quad z_{t+1} = Kz_t, \quad \hat{x}_t = \psi(z_t), \quad (6)$$

where z_t is the encoded latent state and \hat{x}_t is the reconstructed state. To preserve the long-term statistical behaviour of the system and approximate the spectral properties of a measure-preserving dynamical system, we constrain the operator K to be unitary, i.e., $K^\top K = I^{63-65}$. This ensures that the Koopman dynamics in the latent space are norm-preserving and stable under long-term rollouts. In this work, unitarity is imposed by adding a regularisation term to the loss function of the form $\mathcal{L}_{\text{unitary}} = \|K^\top K - I\|^2$. The Koopman operator K evolves the system in a latent Hilbert space of encoded observables, enabling a linear and spectrally coherent representation of the dynamics. However, the preservation of long-term statistical properties in this latent space does not automatically guarantee consistency with the statistical structure of the original physical state space. To address this, we incorporate a QCBM that generates the probability of the system in the physical space. The QCBM-generated distribution serves as a reference against which the physical-

space statistics of long-term rollouts are compared.

To address this, we integrate a QCBM, which approximates the invariant distribution Q-prior $p_\theta(x)$ of the system. This quantum-learned prior is used as a statistical regulariser during surrogate training, guiding the model to produce predictions that are not only temporally coherent but also statistically consistent with the system’s long-term behaviour (See Method C).

While the Koopman is introduced using a generic state variable x , in this work, we focus on predicting physical states u . We use the Koopman operator to predict the next time frame of the physical states \hat{u}_{t+1} . The training loss combines reconstruction fidelity and statistical alignment:

$$\mathcal{L}_{\text{total}} = \mathcal{L}_{\text{recon}} + \mathcal{L}_{\text{unitary}} + \lambda_{\text{KL}}\mathcal{L}_{\text{KL}} + \lambda_{\text{MMD}}\mathcal{L}_{\text{MMD}}, \quad (7)$$

where

$$\mathcal{L}_{\text{recon}} = \|\hat{u}_{t+1} - u_{t+1}\|^2, \quad (8)$$

$$\mathcal{L}_{\text{KL}} = D_{\text{KL}}(\hat{q}(x) \parallel p_\theta(x)), \quad (9)$$

$$\mathcal{L}_{\text{MMD}} = \|\mathbb{E}_{x \sim \hat{q}(x)}[\phi(x)] - \mathbb{E}_{x \sim p_\theta(x)}[\phi(x)]\|_{\mathcal{H}}^2. \quad (10)$$

Here, $\hat{q}(x)$ is the empirical distribution induced by predicted states, $\phi(x)$ denotes a kernel embedding, and $\lambda_{\text{KL}}, \lambda_{\text{MMD}}$ are empirically selected hyperparameters. The KL divergence captures low-order, information-theoretic discrepancies, while the MMD term captures higher-order statistical structure through kernel embeddings. The full QIML framework is demonstrated in Algorithm 1. All models are implemented in PyTorch with fully differentiable integration of Q-priors. Architectural details for predicting 1D and 2D systems are provided in Supplementary Information S7.2 and S7.3.

B. Invariant measure for chaotic systems

The concept of an invariant measure originates from the field of ergodic theory and has become a fundamental tool in the study of dynamical systems. First formalized in the context of measure-preserving transformations by Birkhoff and von Neumann in the early

20th century, invariant measures capture the long-term statistical behaviour of systems evolving under deterministic rules^{66,67}.

An invariant measure describes how a dynamical system spends its time in different regions of its state space over the long term. For a system evolving under a map T , the invariant measure $\mu(x)$ satisfies:

$$\mu(T^{-1}(A)) = \mu(A), \tag{11}$$

which means that the total probability of the system being in a region A remains the same after one step of evolution. This property reflects a kind of statistical balance: although individual trajectories may change, the overall distribution stays stable. In our work, we aim to capture this long-term behaviour by ensuring that the model’s predictions remain consistent with a reference distribution, which we learn using a QCBM.

In turbulent flows, such invariant measures typically manifest as conserved distributions, such as velocity probability, turbulent kinetic energy or energy spectra that encode physical long-term steady states. Capturing these invariant features is essential for ensuring robustness in extrapolative prediction regimes, where a classical machine learning method often suffers from gradient explosion, mode collapse, or long-term error accumulation⁶⁸.

Algorithm 1 Training of the Quantum-Informed Machine Learning Model

Require: Dataset $\{u_t, u_{t+1}\}$, Q-prior distribution $p_\theta(x)$

- 1: Initialise surrogate model parameters ϕ
- 2: Set loss weights $\lambda_{\text{KL}}, \lambda_{\text{MMD}}$
- 3: **for** each training epoch **do**
- 4: **for** each mini-batch (u_t, u_{t+1}) **do**
- 5: Predict next-step field: $\hat{u}_{t+1} \leftarrow f_\phi(u_t, \dots)$
- 6: Compute empirical distribution $\hat{q}(x)$ from \hat{u}_{t+1}
- 7: Compute reconstruction loss: $\mathcal{L}_{\text{recon}} \leftarrow \|\hat{u}_{t+1} - u_{t+1}\|^2$
- 8: Compute KL divergence: $\mathcal{L}_{\text{KL}} \leftarrow D_{\text{KL}}(\hat{q}(x) \| p_\theta(x))$
- 9: Compute MMD loss: $\mathcal{L}_{\text{MMD}} \leftarrow \|\mathbb{E}_{x \sim \hat{q}(x)}[\phi(x)] - \mathbb{E}_{x \sim p_\theta(x)}[\phi(x)]\|_{\mathcal{H}}^2$
- 10: Compute total loss:

$$\mathcal{L}_{\text{total}} = \mathcal{L}_{\text{recon}} + \lambda_{\text{KL}} \mathcal{L}_{\text{KL}} + \lambda_{\text{MMD}} \mathcal{L}_{\text{MMD}}$$

- 11: Backpropagate and update ϕ via Adam optimizer
 - 12: **end for**
 - 13: **end for**
 - 14: **return** Trained model f_ϕ
-

C. The quantum circuit Born machine to learn the Q-prior

We develop a quantum-informed learning component in which a QCBM is used to directly learn invariant statistical properties from high-dimensional physical observations. The QCBM defines a parameterised quantum state $|\psi_\theta\rangle$ on an n -qubit register, which serves as a generative model over a discretised spatial domain. It does not encode a specific state (e.g., a velocity field) into the circuit. Instead, by observing many snapshots of the system, it learns to reproduce their underlying invariant probability distribution. Specifically, each computational basis state $x \in \{0, 1\}^n$ here is mapped bijectively to a spatial coordinate in the simulation grid. The corresponding amplitude $\langle x | \psi_\theta \rangle$ is optimised so that its squared magnitude approximates the normalised velocity magnitude at that point. Although the circuit does not encode classical inputs directly via amplitude encoding, it constructs a quantum state whose Born distribution approximates the invariant measure Q-prior of the

system. The resulting Born distribution is given by:

$$p_{\theta}(x) = |\langle x|U(\theta)|0\rangle^{\otimes n}|^2, \quad (12)$$

where $U(\theta)$ is a parameterised unitary circuit composed of L layers, each consisting of single-qubit rotations and entangling operations. Each computational basis state represents a discrete spatial point, and the quantum amplitudes are trained to reflect the empirical distribution of local velocity magnitudes. This provides a compact, data-driven mapping from physical observables into the Hilbert space, where complex correlations can be more effectively represented. Further details can be found in S1.3 and other sections in the Supplementary Information.

As shown in Algorithm 2, the QCBM is trained as a quantum generative model. Each computational basis state $x \in \{0, 1\}^n$ is mapped uniquely to a spatial location \mathbf{r}_x in the discretised velocity field, and its target value is the corresponding velocity magnitude $u(\mathbf{r}_x)$. Because the underlying probability distribution over spatial locations is unknown, we adopt a sample-based training strategy that minimises the Maximum Mean Discrepancy (MMD):

$$\mathcal{L}_{\text{MMD}}(\theta) = \left\| \frac{1}{N} \sum_{i=1}^N \phi(x_i) - \frac{1}{M} \sum_{j=1}^M \phi(\tilde{x}_j) \right\|_{\mathcal{H}}^2, \quad (13)$$

Here, $\{x_i\}_{i=1}^N$ denotes the batch of empirical samples drawn from the reference velocity field, while $\{\tilde{x}_j\}_{j=1}^M \sim p_{\theta}(x)$ are samples generated by the QCBM. Because the MMD objective is expressed solely through kernel evaluations on finite sample sets, optimisation of the QCBM requires no closed-form expression for the target probability density. This sample-based objective is particularly advantageous for high-dimensional chaotic flows, where the invariant measure is available only as a time-ordered set of simulation snapshots rather than an explicit probability density. By aligning the QCBM's samples with these empirical trajectories, the model infers the underlying measure without ever needing a closed-form expression.

Algorithm 2 Training of the QCBM for invariant measure

Require: Velocity snapshots $\{u_t\}$; circuit depth L ; qubits n

Ensure: Optimised parameters θ^* such that $p_{\theta^*}(x)$ matches the empirical distribution

- 1: Initialise $\theta \sim \mathcal{U}[-\pi, \pi]$
 - 2: **for each** training epoch **do**
 - 3: Build unitary $U(\theta)$ (depth L , n qubits)
 - 4: Generate M samples $\{\tilde{x}_j\}_{j=1}^M \sim p_{\theta}(x)$
 - 5: Extract N target samples $\{x_i\}_{i=1}^N$ from $\{u_t\}$
 - 6: Compute $\mathcal{L}_{\text{MMD}}(\{x_i\}, \{\tilde{x}_j\})$
 - 7: $\theta \leftarrow \theta - \eta \nabla_{\theta} \mathcal{L}_{\text{MMD}}$
 - 8: **end for**
 - 9: **return** θ^*
-

The trained quantum distribution $p_{\theta}(x)$ thus can serve as a data-driven prior capturing the invariant measure of the underlying physical process. Unlike classical regularisers based on fixed heuristics, the QCBM constructs this Q-prior through optimisation on empirical data.

All quantum circuits are implemented using hardware-efficient structures, which are detailed in Supplementary Information S2.2. Training is carried out on noiseless simulators and on superconducting quantum hardware, with circuit transpilation, error mitigation, and device-specific calibration performed using the Qiskit runtime. Further details and the optimisation methods are provided in Supplementary Information S1.3 & S2.3.

D. Quantum hardware implementation

The QCBM model was trained using both emulators and real superconducting quantum processors. To ensure effective execution on near-term quantum hardware and to manage the impact of noise on the quality of Q-priors, this study constrains the total number of trainable parameters and adopts conservative circuit configurations. Specifically, the number of qubits is limited to 10–15, with circuit depths ranging from 3 to 8 layers, resulting in fewer than 300 trainable parameters in total (detail see: Supplementary Information S2.2-2.3). Hardware experiments were mainly conducted on IQM’s 20-qubit superconducting

chip (Garnet)^{69,70}, using qubits 1–10 as the active subset. Further discussion on hardware sensitivity is provided in Supplementary Sections S2.4 and S2.5. To ensure scalability, the quantum backend was integrated into a GPU-accelerated classical training loop on NVIDIA A100 nodes provided by BEAST GPU cluster (Leibniz Supercomputing Centre). Gradient evaluation, loss computation, and optimiser updates were performed classically and synchronised with the quantum hardware at each iteration. This setup constitutes an applied demonstration of embedding NISQ-era QPUs into scientific machine learning pipelines.

The employed QCBM circuit architecture consisted of alternating layers of parameterised R_x rotations and hardware-native entangling gates. Importantly, the same circuit structure was used across all experiments without dataset-specific tailoring, ensuring general applicability. Although performance could potentially be improved through customised ansatz design, our results demonstrate that the proposed quantum-informed framework is compatible with any hardware-efficient quantum circuit. This adaptability enables the integration of diverse circuit architectures without modifying the overall training pipeline, suggesting broad utility across problem domains and quantum backends.

Each circuit was sampled with 20,000 shots per iteration, and readout errors were mitigated using IQM’s native transpiler and the Mthree measurement mitigation toolkit⁷¹. Optimisation was performed using L-BFGS⁷², Adam, and COBYLA⁷³, selected based on convergence stability and noise robustness. To prevent mode collapse, such as excessive sampling concentration on the $|0\rangle$ state, runtime monitoring and redundancy checks were incorporated into the training loop. Despite operating with only 10 to 15 qubits, the QCBM successfully captured the structure of invariant distributions over a 1000- to 60,000-dimensional Hilbert space, demonstrating the effectiveness of NISQ-compatible priors in modelling high-dimensional systems. Further discussions of the error mitigations, experiment results and ablations are provided in the Supplementary Information S2.5 and S7.

E. Quantum memory efficiency

A defining feature of the proposed framework is its capacity to encode high-dimensional physical information using significantly fewer trainable parameters than conventional deep learning models. The QCBM, operating on only 10–15 qubits and comprising fewer than 300 trainable parameters, successfully captures invariant distributions over spatial domains with

dimensionality exceeding 10^4 . In contrast, a classical neural network capable of learning an equally expressive distribution over the same domain would require at least $\mathcal{O}(10^4)$ parameters, assuming a minimal fully connected architecture with comparable granularity. For example, on a grid of $D = 2^{10} = 1,024$ spatial points, the lightest fully-connected (FC) network that can approximate an arbitrary probability map with standard universal-approximation accuracy must allocate $\Theta(D^2)$ weights^{74,75}. Even with an aggressively thinned hidden layer this still amounts to $\sim 2.5 \times 10^5$ tunable parameters—three orders of magnitude more than the 240 rotation angles used by our ten-qubit QCBM. Moreover, classical models lack access to quantum entanglement, limiting their ability to compactly encode non-local correlations and higher-order statistical dependencies prevalent in turbulent or chaotic systems.

For the turbulent-channel dataset, retaining all 595 mid-plane snapshots in double precision requires roughly 5.0×10^2 MB. Archiving the corresponding QCBM checkpoint for each snapshot (4.3 kB per file) occupies only $595 \times 4.3 \text{ kB} \approx 2.5$ MB, a compression greater than two orders of magnitude while preserving the relevant flow statistics. Comparable savings are obtained for Kolmogorov flow (~ 180 parameters, ~ 1.4 kB per file, ~ 0.44 MB in total) and Kuramoto-Sivashinsky data (~ 120 parameters, ~ 1 kB per file, ~ 1.4 MB in total). Full storage calculations are shown and reported in Supplementary Information S8. Such dramatic savings make the Q-prior attractive whenever data are expensive to generate or archive, while still providing a statistically faithful, low-parameter regulariser for the classical Koopman surrogate.

The quantum module’s ability to generate a faithful statistical prior with such a compact parameterisation highlights its potential as a highly efficient generative component within hybrid learning pipelines. This parameter efficiency is particularly relevant in scientific domains where data are sparse or expensive to obtain and store, and where encoding physical constraints is essential for generalisability.

V. DATA AVAILABILITY

All data needed to evaluate the conclusions in the paper are present in the paper and/or the Supplementary Information S4. The training/validation/testing datasets for all three cases are available on <https://doi.org/10.5281/zenodo.16419085>.

VI. CODE AVAILABILITY

The complete training code for the QCBM module and the Koopman surrogate model is openly available at the <https://github.com/UCL-CCS/QIML.git>.

REFERENCES

- ¹L. Biferale, G. Boffetta, A. Celani, B. Devenish, A. Lanotte, and F. Toschi, “Multifractal statistics of lagrangian velocity and acceleration in turbulence,” *Physical Review Letters* **93**, 064502 (2004).
- ²V. A. Galaktionov and J. L. Vázquez, *A stability technique for evolution partial differential equations: a dynamical systems approach*, Vol. 56 (Springer Science & Business Media, 2012).
- ³Z. Long, Y. Lu, X. Ma, and B. Dong, “Pde-net: Learning pdes from data,” in *International conference on machine learning* (PMLR, 2018) pp. 3208–3216.
- ⁴H. Bergström, H. Alfredsson, J. Arnqvist, I. Carlén, E. Dellwik, J. Fransson, H. Ganander, M. Mohr, A. Segalini, and S. Söderberg, “Wind power in forests: wind and effects on loads,” (2013).
- ⁵P. V. Coveney, “Sharkovskii’s theorem and the limits of digital computers for the simulation of chaotic dynamical systems,” *Journal of Computational Science* **83**, 102449 (2024).
- ⁶M. Klöwer, P. V. Coveney, E. A. Paxton, and T. N. Palmer, “Periodic orbits in chaotic systems simulated at low precision,” *Scientific Reports* **13**, 11410 (2023).
- ⁷B. M. Boghosian, P. V. Coveney, and H. Wang, “A new pathology in the simulation of chaotic dynamical systems on digital computers,” *Advanced Theory and Simulations* **2**, 1900125 (2019).
- ⁸P. V. Coveney and S. Wan, *Molecular Dynamics: Probability and Uncertainty* (Oxford University Press, 2025).
- ⁹D. Kalla, N. Smith, F. Samaah, and S. Kuraku, “Study and analysis of chat gpt and its impact on different fields of study,” *International journal of innovative science and research technology* **8** (2023).
- ¹⁰E. Kasneci, K. Seßler, S. Küchemann, M. Bannert, D. Dementieva, F. Fischer, U. Gasser, G. Groh, S. Günemann, E. Hüllermeier, *et al.*, “ChatGPT for good? on opportunities

- and challenges of large language models for education,” *Learning and individual differences* **103**, 102274 (2023).
- ¹¹Y. Chang, X. Wang, J. Wang, Y. Wu, L. Yang, K. Zhu, H. Chen, X. Yi, C. Wang, Y. Wang, *et al.*, “A survey on evaluation of large language models,” *ACM transactions on intelligent systems and technology* **15**, 1–45 (2024).
- ¹²A. J. Thirunavukarasu, D. S. J. Ting, K. Elangovan, L. Gutierrez, T. F. Tan, and D. S. W. Ting, “Large language models in medicine,” *Nature medicine* **29**, 1930–1940 (2023).
- ¹³A. Voulodimos, N. Doulamis, A. Doulamis, and E. Protopapadakis, “Deep learning for computer vision: A brief review,” *Computational intelligence and neuroscience* **2018**, 7068349 (2018).
- ¹⁴J. Zhang, J. Huang, S. Jin, and S. Lu, “Vision-language models for vision tasks: A survey,” *IEEE transactions on pattern analysis and machine intelligence* **46**, 5625–5644 (2024).
- ¹⁵K. Zhou, J. Yang, C. C. Loy, and Z. Liu, “Learning to prompt for vision-language models,” *International Journal of Computer Vision* **130**, 2337–2348 (2022).
- ¹⁶P. Zhang, X. Li, X. Hu, J. Yang, L. Zhang, L. Wang, Y. Choi, and J. Gao, “Vinvl: Revisiting visual representations in vision-language models,” in *Proceedings of the IEEE/CVF conference on computer vision and pattern recognition* (2021) pp. 5579–5588.
- ¹⁷I. Price, A. Sanchez-Gonzalez, F. Alet, T. R. Andersson, A. El-Kadi, D. Masters, T. Ewalds, J. Stott, S. Mohamed, P. Battaglia, *et al.*, “Probabilistic weather forecasting with machine learning,” *Nature* **637**, 84–90 (2025).
- ¹⁸K. Bi, L. Xie, H. Zhang, X. Chen, X. Gu, and Q. Tian, “Accurate medium-range global weather forecasting with 3d neural networks,” *Nature* **619**, 533–538 (2023).
- ¹⁹R. Lam, A. Sanchez-Gonzalez, M. Willson, P. Wirnsberger, M. Fortunato, F. Alet, S. Ravuri, T. Ewalds, Z. Eaton-Rosen, W. Hu, *et al.*, “Learning skillful medium-range global weather forecasting,” *Science* **382**, 1416–1421 (2023).
- ²⁰M. Cavaiola, F. Cassola, D. Sacchetti, F. Ferrari, and A. Mazzino, “Hybrid ai-enhanced lightning flash prediction in the medium-range forecast horizon,” *Nature Communications* **15**, 1188 (2024).
- ²¹S. L. Brunton, B. R. Noack, and P. Koumoutsakos, “Machine learning for fluid mechanics,” *Annual Review of Fluid Mechanics* **52**, 477–508 (2020).
- ²²H. J. Bae and P. Koumoutsakos, “Scientific multi-agent reinforcement learning for wall-models of turbulent flows,” *Nature Communications* **13**, 1443 (2022).

- ²³X. Yang, S. Zafar, J.-X. Wang, and H. Xiao, “Predictive large-eddy-simulation wall modeling via physics-informed neural networks,” *Physical Review Fluids* **4**, 034602 (2019).
- ²⁴X. Xue, S. Wang, H.-D. Yao, L. Davidson, and P. V. Coveney, “Physics informed data-driven near-wall modelling for lattice Boltzmann simulation of high reynolds number turbulent flows,” *Communications Physics* **7**, 338 (2024).
- ²⁵R. Maulik, O. San, J. D. Jacob, and C. Crick, “Sub-grid scale model classification and blending through deep learning,” *Journal of Fluid Mechanics* **870**, 784–812 (2019).
- ²⁶A. Pal, “Deep learning emulation of subgrid-scale processes in turbulent shear flows,” *Geophysical Research Letters* **47**, e2020GL087005 (2020).
- ²⁷K. Fukami, Y. Nabae, K. Kawai, and K. Fukagata, “Synthetic turbulent inflow generator using machine learning,” *Physical Review Fluids* **4**, 064603 (2019).
- ²⁸M. Z. Yousif, L. Yu, and H. Lim, “Physics-guided deep learning for generating turbulent inflow conditions,” *Journal of Fluid Mechanics* **936**, A21 (2022).
- ²⁹M. Raissi, P. Perdikaris, and G. E. Karniadakis, “Physics-informed neural networks: A deep learning framework for solving forward and inverse problems involving nonlinear partial differential equations,” *Journal of Computational physics* **378**, 686–707 (2019).
- ³⁰I. Goodfellow, J. Pouget-Abadie, M. Mirza, B. Xu, D. Warde-Farley, S. Ozair, A. Courville, and Y. Bengio, “Generative adversarial networks,” *Communications of the ACM* **63**, 139–144 (2020).
- ³¹L. Lu, P. Jin, G. Pang, Z. Zhang, and G. E. Karniadakis, “Learning nonlinear operators via deep neural networks based on the universal approximation theorem of operators,” *Nature Machine Intelligence* **3**, 218–229 (2021).
- ³²Z. Li, N. Kovachki, K. Azizzadenesheli, B. Liu, K. Bhattacharya, A. Stuart, and A. Anandkumar, “Fourier neural operator for parametric partial differential equations,” arXiv preprint arXiv:2010.08895 (2020).
- ³³V. Vanchurin, “Toward a theory of machine learning,” *Machine Learning: Science and Technology* **2**, 035012 (2021).
- ³⁴G. Carleo, I. Cirac, K. Cranmer, L. Daudet, M. Schuld, N. Tishby, L. Vogt-Maranto, and L. Zdeborová, “Machine learning and the physical sciences,” *Reviews of Modern Physics* **91**, 045002 (2019).
- ³⁵Y. Schiff, Z. Y. Wan, J. B. Parker, S. Hoyer, V. Kuleshov, F. Sha, and L. Zepeda-Núñez, “Dyslim: Dynamics Stable Learning by Invariant Measure for Chaotic Systems,” arXiv

- preprint arXiv:2402.04467 (2024).
- ³⁶X. Gao, E. R. Anschuetz, S.-T. Wang, J. I. Cirac, and M. D. Lukin, “Enhancing generative models via quantum correlations,” *Physical Review X* **12**, 021037 (2022).
- ³⁷J. Tilly, H. Chen, S. Cao, D. Picozzi, K. Setia, Y. Li, E. Grant, L. Wossnig, I. Rungger, G. H. Booth, *et al.*, “The variational quantum eigensolver: a review of methods and best practices,” *Physics Reports* **986**, 1–128 (2022).
- ³⁸A. Kandala, A. Mezzacapo, K. Temme, M. Takita, M. Brink, J. M. Chow, and J. M. Gambetta, “Hardware-efficient variational quantum eigensolver for small molecules and quantum magnets,” *nature* **549**, 242–246 (2017).
- ³⁹R. Babbush, C. Gidney, D. W. Berry, N. Wiebe, J. McClean, H. Neven, A. White, and A. Komar, “Quantum algorithm for chemistry with low-degree polynomial scaling,” *Physical Review Letters* **120**, 110501 (2018).
- ⁴⁰M. Reiher, N. Wiebe, K. M. Svore, D. Wecker, and M. Troyer, “A quantum algorithm for the simulation of molecular energies,” *Physical Review Letters* **124**, 010501 (2020).
- ⁴¹J. Stokes, J. Izaac, N. Killoran, and G. Carleo, “Quantum natural gradient,” *Quantum* **4**, 269 (2020).
- ⁴²E. Farhi, J. Goldstone, and S. Gutmann, “Quantum approximate optimization algorithm,” *Physical Review X* **6**, 031007 (2014).
- ⁴³A. Lucas, “Ising formulations of the travelling salesman problem and other np-hard problems,” *Frontiers in Physics* **4**, 51 (2014).
- ⁴⁴M. G. Vakili, C. Gorgulla, A. Nigam, D. Bezrukov, D. Varoli, A. Aliper, D. Polykovsky, K. M. P. Das, J. Snider, A. Lyakisheva, *et al.*, “Quantum computing-enhanced algorithm unveils novel inhibitors for kras,” arXiv preprint arXiv:2402.08210 (2024).
- ⁴⁵J. Romero and A. Aspuru-Guzik, “Variational quantum generators: Generative adversarial quantum machine learning for continuous distributions,” *Advanced Quantum Technologies* **4**, 2000003 (2021).
- ⁴⁶P.-L. Dallaire-Demers and N. Killoran, “Quantum generative adversarial networks,” *Physical Review Applied* **8**, 024012 (2018).
- ⁴⁷M. Benedetti, M. Fiorentini, L. P. Garcia-Pintos, E. M. Stoudenmire, A. Zlokapa, and A. Perdomo-Ortiz, “Learning a quantum spin model with a quantum computer,” *Nature Physics* **14**, 693–698 (2018).
- ⁴⁸J. Preskill, “Quantum computing in the NISQ era and beyond,” *Quantum* **2**, 79 (2018).

- ⁴⁹T. Kubař, M. Elstner, and Q. Cui, “Hybrid quantum mechanical/molecular mechanical methods for studying energy transduction in biomolecular machines,” *Annual Review of Biophysics* **52**, 525–551 (2023).
- ⁵⁰C. Kühne, P. Gkeka, D. Zobel, K. Reuter, and A. Tkatchenko, “Machine learning for QM/MM approaches,” *Annual Review of Physical Chemistry* **73**, 527–550 (2022).
- ⁵¹H. M. Senn and W. Thiel, “QM/MM methods for enzyme catalysis: Challenges and advances,” *Chemical Reviews* **121**, 10178–10214 (2021).
- ⁵²T. M. Bickley, A. Mingare, T. Weaving, M. W. de la Bastida, S. Wan, M. Nibbi, P. Seitz, A. Ralli, P. J. Love, M. Chung, *et al.*, “Extending quantum computing through subspace, embedding and classical molecular dynamics techniques,” arXiv preprint arXiv:2505.16796 (2025).
- ⁵³J.-G. Liu and L. Wang, “Differentiable learning of quantum circuit born machines,” *Physical Review A* **98**, 062324 (2018).
- ⁵⁴M. Benedetti, E. Lloyd, S. Mohan, E. M. Stoudenmire, and A. Perdomo-Ortiz, “A generative modeling approach for benchmarking and training shallow quantum circuits,” *npj Quantum Information* **5**, 45 (2019).
- ⁵⁵A. Gretton, K. M. Borgwardt, M. J. Rasch, B. Schölkopf, and A. Smola, “A kernel two-sample test,” *The Journal of Machine Learning Research* **13**, 723–773 (2012).
- ⁵⁶G. Freire, M. Coelho, C. Osthoff, and K. Ocaña, “Análise de desempenho do beast 1.10 em ambientes de hpc: Explorando cpu, gpu, multi-gpu,” in *Simpósio em Sistemas Computacionais de Alto Desempenho (SSCAD)* (SBC, 2024) pp. 73–80.
- ⁵⁷M. Cerezo, G. Verdon, H.-Y. Huang, L. Cincio, and P. J. Coles, “Challenges and opportunities in quantum machine learning,” *Nature Computational Science* **2**, 567–576 (2022).
- ⁵⁸S. Succi, *The Lattice Boltzmann Equation for Fluid Dynamics and Beyond* (Oxford University Press, 2001).
- ⁵⁹R. D. Moser, J. Kim, and N. N. Mansour, “Direct numerical simulation of turbulent channel flow up to $re_\tau = 590$,” *Physics of Fluids* **11**, 943–945 (1999).
- ⁶⁰S. Chen and G. D. Doolen, “Lattice Boltzmann method for fluid flows,” *Annual Review of Fluid Mechanics* **30**, 329–364 (1998).
- ⁶¹X. Xue, H.-D. Yao, and L. Davidson, “Synthetic turbulence generator for lattice Boltzmann method at the interface between rans and LES,” *Physics of Fluids* **34**, 055118 (2022).

- ⁶²C. S. Calude and G. Longo, “The deluge of spurious correlations in big data,” *Foundations of science* **22**, 595–612 (2017).
- ⁶³K. E. Petersen and K. Petersen, *Ergodic theory* (Cambridge university press, 1989).
- ⁶⁴M. Budišić, R. Mohr, and I. Mezić, “Applied koopmanism,” *Chaos: An Interdisciplinary Journal of Nonlinear Science* **22** (2012).
- ⁶⁵X. Cheng, Y. He, Y. Yang, X. Xue, S. Cheng, D. Giles, X. Tang, and Y. Hu, “Learning chaos in a linear way,” arXiv preprint arXiv:2503.14702 (2025).
- ⁶⁶G. D. Birkhoff, “Proof of the ergodic theorem,” *Proceedings of the National Academy of Sciences* **17**, 656–660 (1931).
- ⁶⁷J. von Neumann, “Proof of the quasi-ergodic hypothesis,” *Proceedings of the National Academy of Sciences* **18**, 70–82 (1932).
- ⁶⁸R. Pascanu, T. Mikolov, and Y. Bengio, “On the difficulty of training recurrent neural networks,” in *International conference on machine learning* (2013) pp. 1310–1318.
- ⁶⁹F. Marxer, A. Vepsäläinen, S. W. Jolin, J. Tuorila, A. Landra, C. Ockeloen-Korppi, W. Liu, O. Ahonen, A. Auer, L. Belzane, *et al.*, “Long-distance transmon coupler with cz-gate fidelity above 99.8%,” *PRX Quantum* **4**, 010314 (2023).
- ⁷⁰L. Abdurakhimov, J. Adam, H. Ahmad, O. Ahonen, M. Algaba, G. Alonso, V. Bergholm, R. Beriwal, M. Beuerle, C. Bockstiegel, *et al.*, “Technology and performance benchmarks of iqm’s 20-qubit quantum computer,” arXiv preprint arXiv:2408.12433 (2024).
- ⁷¹P. D. Nation, H. Kang, N. Sundaresan, and J. M. Gambetta, “Scalable mitigation of measurement errors on quantum computers,” *PRX Quantum* **2**, 040326 (2021).
- ⁷²C. Zhu, R. H. Byrd, P. Lu, and J. Nocedal, “Algorithm 778: L-bfgs-b: Fortran subroutines for large-scale bound-constrained optimization,” *ACM Transactions on mathematical software (TOMS)* **23**, 550–560 (1997).
- ⁷³R. G. Regis, “Stochastic radial basis function algorithms for large-scale optimization involving expensive black-box objective and constraint functions,” *Computers & Operations Research* **38**, 837–853 (2011).
- ⁷⁴A. R. Barron, “Universal approximation bounds for superpositions of a sigmoidal function,” *IEEE Trans. Inf. Theory* **39**, 930–945 (1993).
- ⁷⁵I. Goodfellow, Y. Bengio, and A. Courville, *Deep Learning* (MIT Press, 2016) Chap. 6.

VII. ACKNOWLEDGEMENTS

We acknowledge funding support from European Commission CompBioMed Centre of Excellence (Grant No. 675451 and 823712). Support from the UK Engineering and Physical Sciences Research Council under the projects “UK Consortium on Mesoscale Engineering Sciences (UKCOMES)” (Grant No. EP/R029598/1) and “Software Environment for Actionable and VVUQ-evaluated Exascale Applications (SEAVEA)” (Grant No. EP/W007711/1) is gratefully acknowledged. 2024-2025 DOE INCITE award for computational resources on supercomputers at the Oak and Argonne Leadership Computing Facility under the “COMP-BIO3” project. We also gratefully acknowledge IQM Quantum Computers for providing access to superconducting quantum processors used in hardware benchmarking, and the Leibniz Supercomputing Centre (LRZ) for access to the BEAST GPU cluster, which supported the training of classical models and quantum circuit simulations.

VIII. CONTRIBUTIONS

M.W. and X.X. jointly conceived the central idea of the study and collaboratively designed the quantum-informed machine learning framework. Both authors conducted the quantum hardware experiments and contributed equally to the classical modelling and validation. M.W. led the writing of the quantum algorithm and hardware implementation sections, while X.X. was responsible for drafting the classical modelling and chaotic system descriptions. Data analysis, hyperparameter tuning, and visualisation were carried out jointly by M.W. and X.X. P.V.C. provided guidance throughout the experimental design, software and hardware execution and optimisation processes. All authors discussed the results and contributed to the final manuscript.

IX. COMPETING OF INTERESTS

The authors declare no competing interests.